J Ther Eng, Vol. 10, No. 5, pp. 1275−1291, September, 2024

Journal of Thermal Engineering
Web page info: https://jten.yildiz.edu.tr
DOI: 10.14744/thermal.0000866

Research Article

Experimental and computational study of heat transfer and flow structure of slotted impinging jet

S. Mohamed ILLYAS[1,*], B. R. Ramesh BAPU[2], A. Muthu MANOKAR[1]

[1]*Department of Mechanical Engineering, B S Abdur Rahman Crescent Institute of Science and Technology, Chennai, 600048, India*
[2]*Department of Mechanical Engineering, Prathyusha Engineering College, Chennai, 602025, India*

ARTICLE INFO

Article history
Received: 18 June 2022
Revised: 16 September 2022
Accepted: 10 October 2022

Keywords:
Flow Structure; Heat Transfer Enhancement; Numerical Simulation; Slotted Jet; Thermochromic Liquid Crystal

ABSTRACT

The study is focused on the flow parameters of the slotted impinging jet associated with its heat transfer performance. The analysis is performed for the circular and slotted jets of square, cross, and oval sections for flow outlet to target plate distance of L/D = 1 to 4. The Reynolds number range of 12700 – 23000 is used in this study to analyze the heat transfer pattern using liquid crystal sheet. The numerical analysis is carried out using CFD. The axial velocity peak (u/U_0 = 2.124) is observed for the square jet corresponding to r/D = 0.33 at L/D = 1 and the peak reduces with increasing L/D distances. Higher intensity of average radial velocity (u_r/U_0 = 1.44) is observed close to the impinging plate for the slotted jet at L/D = 1 at 0.5 ≤ r/D ≤ 1.4 compared with radial velocity (u_r/U_0 = 0.91) of circular jet. Nusselt number distribution has little dependence for circular jet on the separation distance as the variation is marginal at L/D = 4 when compared to L/D = 1 and 2, the slotted jet however shows marked variation of Nusselt number (136.8 at L/D = 1, 135.2 at L/D = 2 and 113.5 at L/D = 4) in the region at X/D = 1.5. The highest values of turbulence intensity (TI = 0.206) is observed at r/D = 0.5 for the square jet at L/D = 3.

Cite this article as: Illyas SM, Bapu BRR, Manokar AM. Experimental and computational study of heat transfer and flow structure of slotted impinging jet. J Ther Eng 2024;10(5):1275−1291.

INTRODUCTION

Impinging jet has evolved as a primary source for controlled cooling as well as heating of a surface due to its ability to improve the heat transfer rate for of drying of food products and electronic components cooling. The flow parameters of air jet are complex in nature and subsequently, heat transfer from the surface is significantly variable. The impinging jet has the advantage of high transfer rate than other heat transfer applications. Because of this reason, heat transfer by jet impingement has attracted extensive research.

Wang et al. [1] examined the flow and heat parameter of jets over a flat surface with orifice configurations of circular, elliptic, and square aspect ratios 3-5. They reported the existence of axis switching vortex rings for rectangular and elliptic jets before the impingement and it enhances turbulence and heat compared with uniform section air jet. They concluded that the rectangular orifice of aspect ratio

***Corresponding author.**
*E-mail address: illyasmech4@gmail.com

This paper was recommended for publication in revised form by Associate Editor Erman Aslan

5 provides better cooling performance. Zhu et al. [2] investigated the heat parameter of nozzles with velocity differences among adjacent jets. The results revealed that Re_{ratio} is the primary factor influencing the uniform heat parameter. They reported improved heat parameter of multi nozzles on comparison to single slot nozzle. Afroz and Sharif [3] numerically analyzed the heat parameter of air jets (Swirl number Sw = 0 -0.77) with varying H/D distances (0.5 – 4) and Blockage ratios (0.4 - 0.6). They stated that at the jet area, the velocity parameter is distributed radially and is substantial around the jet axis. Their results revealed that the swirling effect enhances heat transfer at a lower separation distance (H/D = 0.5) compared with uniform section air jet. The peak Nusselt value is initially reduced at higher H/D distances and increases with the increase in swirling effect.

The analysis by Fenot et al. [4] comprehensively examined the heat and flow structure of quasi-annular jets with infrared thermography and PIV techniques. They considered the blockage ratio (ratio of inner diameter and outer diameter – D_i/D_o = 0.35 – 0.85) as the principal parameter and concluded that the existence of shear layer at jet main flow edge causing higher heat parameter. They determined that a higher blockage ratio enhances the entrainment of ambient air before the impingement. Yadav and Saini [5] numerically analyzed the performance of solar heater by jet cooling method (Re = 3500 - 17500). They reported increased heat transfer at the impinging jet area due to by the shearing of air and jet which breaks the boundary layer on the absorber surface. Mohammed and Razuqi [6] studied the heat parameter of a sink provided with air jet. Their study focused on the effect of fan location with constant heat flux varying between 10000–40000 kW/m^2 and Reynolds number range of 3400 – 16000. They concluded that a decrease in thermal resistances with rise in Reynolds number for the cut-out template due to the higher turbulence of airflow. Badiger et al. [7] experimentally analyzed the influence of swirl on heat parameter of a jet on a flat vertical surface. They employed the twisted tape insert (Swirl number Sw = 0.52) with Reynolds number between 1000 and 2500. They reported that the position of impinging plate concerning the inner reaction zone of the inverse diffusion flame influences the intensity of heat parameter to the striking plate. Mohammed and Razuqi [8] analysed the heat parameter of a heat sink with air jet. Their study focused on a processor with a heat sink with closely packed rectangular fins with varying heat flux (10000-70000 kW/m^2) for a Reynolds number range between 4000 and 16000. The results reveal that the fins aligned in the core exhibited a larger temperature gradient compared to the fins that are inline around the core. They reported decreased thermal resistance with an increase in Reynolds value and increased Nusselt value when the Reynolds value and heat flux are increased.

The study by Lee et al. [9] reported the impact of configuration of pipe on flow and heat parameter for Re = 23000 with L/D = 2 - 14. The study showed that the Nusselt value is high with larger pipe diameter at $0 \leq r/D \leq 0.5$ and its effect is marginal at the vicinity of wall jet. The local change in heat parameter for circular air jet on a striking surface (Re = 12000 - 18000 and L/D = 0.5 - 8) is analyzed by Katti and Prabhu [10] revealing that stagnation Nusselt number increases with a low value of L/D below 1 because of accelerating flow and the existence of Nusselt number for L/D distance below 3. Yan et al. [11] carried out an analysis on a jet array with an elliptical cross-section with an aspect ratio of 0.25, 0.5,1,2 and 4 using the liquid crystal technique showing that axial change of impingement position is significant at aspect ratio > 1. A minimum stagnation zone in the Nusselt value was apparent by Lytle and Webb [12] for jet exit and surface distance, $L/D < 0.25$. They revealed that the inner peak disappears beyond L/D = 0.25 and radially leaving jet and stagnant ambient at decreasing L/D distance causes higher turbulence in the boundary layer resulting in outer peak Nusselt number. The velocity parameter at vicinity of the impinging plate and its impact on the Nusselt value of the laminar jet (Re = 100 - 500) issuing from rectangular slots (aspect ratio = 1 - 8.1) were numerically analyzed by Sezai and Mohamad [13]. They reported that the upstream flow from a rectangular slot creates a curvature of streamlines resulting in an off-center velocity peak near the impinging surface. Alekseenko and Bilsky [14] studied the spatial distribution of velocity considering impinging jets with a varying swirl at L/D = 3. Their analysis showed that the existence of vortex was apparent (S = 0.7 – 1).

However, the development of the air jet and the heat parameter on wall may be affected by the upstream entry conditions of the slotted air jet, the underlying flow parameters has not yet been revealed in most of the heat parameter studies [2-12,22] of the impinging jet. Ianiro and Cardone [15] investigate and reported that the swirling jet produces a stronger axial recirculation region causing low heat transfer zones which demands a comprehensive study of flow characteristics. While the flow at the pipe outlet alters the jet spreading rate and turbulence characteristics before it impinges on the surface [16], it is essential to analyze those effects on flows and heat parameter of the impinging jet can be made. Therefore, in the present analysis, a comprehensive study on heat parameter and flow structure of slotted jet impingement is studied with different jet configurations. The study includes the jet configuration of the square, cross, and oval for L/D distances of 1 to 4. The performance of a slotted jet has also been compared with a circular jet. The analysis includes a flow parameter study on axial velocity, velocity vectors, and level of turbulence.

However, the heat parameter studies of the air jet are employed thermocouples for measuring the surface temperature which can measure only on discrete points, the thermo-chromic liquid crystal sheet used in the present study enables to calculate the temperature variation over the surface. In addition, the reported studies of impinging jets show that the small change in nozzle exit flow structure

will have a significant influence on heat parameter on the target plate. While the studies on circular and swirling jets either the diameter of the pipe or the swirling effects are varied with the same insert, the present study focuses on jets with different configurations which provide the scope for analysing the flow parameters and its influence on heat parameter.

While the current analysis provides information on the single jet, the inference from this analysis can be used to understand the heat and flow characteristics with multiple jet arrangements. This may provide the prospect of optimizing the jet arrangement with a combined geometry effect.

EXPERIMENTAL METHODOLOGY

Experimental Setup

The physical setup consists of an air jet issuing facility and target surface as shown in Figures 1 and 2. The jet issuing facility has a 1.5 HP high-pressure centrifugal blower (Figure 1c) that delivers air to a 108 mm diameter converging pipe. The centrifugal blower is preferred for reasonable flow steadiness and a large volume of flow conditions. The converging pipe connecting the blower outlet minimizes both mean and fluctuating velocity variations in the flow without change in its total pressure [17]. The main piping network has a length of about a minimum of 20*D* (Upstream length, L_U =1130 mm) upstream of the venturi meter (Figure 1a) ensuring that flow has fully developed and about 15*D* (Downstream length, L_D = 520 mm) at the downstream to let the effects of venturi contraction to settle. The venturi meter is tapped at its upstream and downstream to connect with a U-tube manometer. A Venturi meter (throat diameter = 20 mm) measures the air flow rate between the two main pipeline sections by a pressure differential. The flow regulating valve located at nozzle pipe controls the air flow rate.

The vertical target surface was made of SS foil (SUS 304) having a size of 300 x 300 x 3 as shown in Figure 1b. The thin heater and SS foil are secured with screws over the acrylic plate measuring 450 mm by 450 mm by 12 mm. The power supply unit's wide range of voltage and current variations.

with fine control unit enables the imposition of the heat flux with a narrow working temperature limit (30°- 46°C) of the TLC sheet. A digital camera with a computer system is employed to capture the liquid crystal sheets. The profile of the slotted sections is shown in Figure 3.

Thermochromic Liquid Crystal Sheet

Thermo-chromic liquid crystal (TLC) sheets are supplied by M/s. Hallcrest exhibiting the RGB color spectrum is used in the analysis. The TLC utilized in this investigation has a bandwidth of R30C5W. Between 30 and 35 degrees Celsius is the temperature range in which the Hallcrest

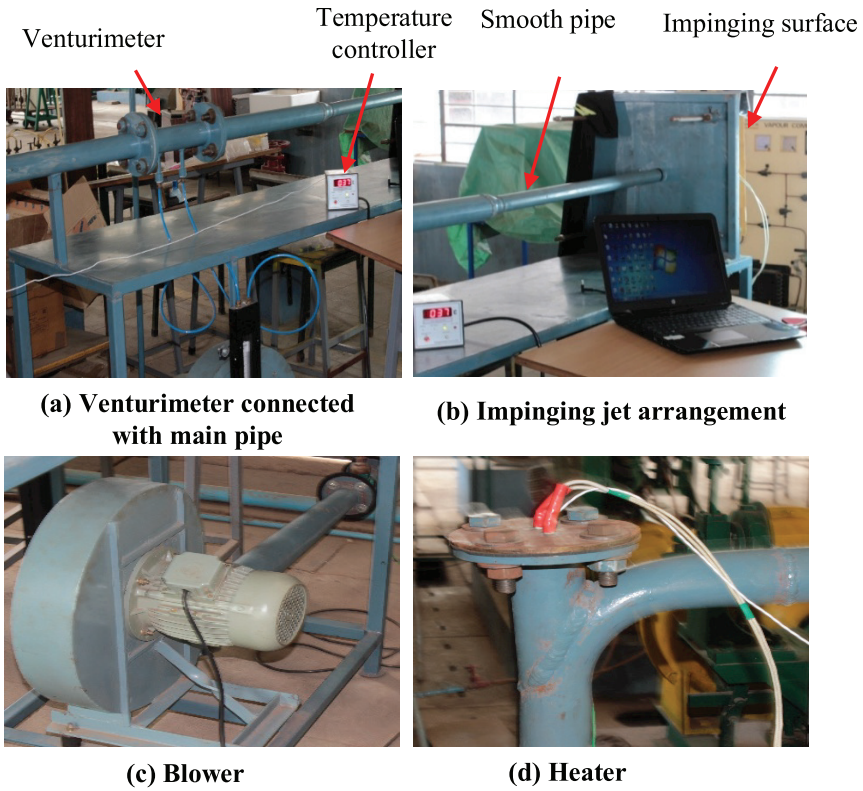

Figure 1. Photographic view of the experimental setup.

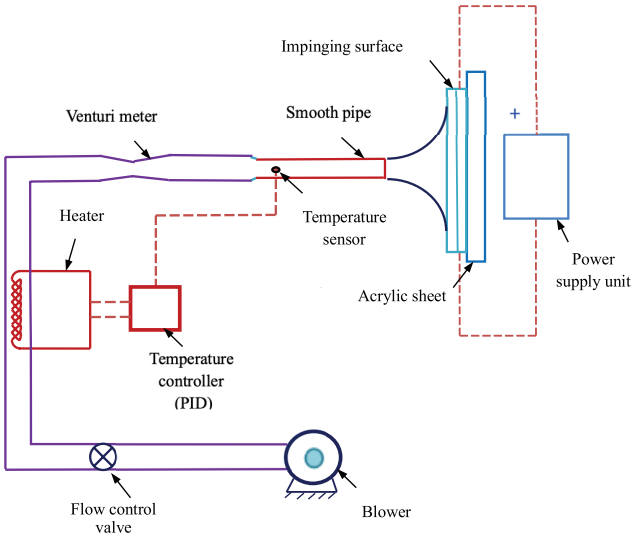

Figure 2. Schematic of an experimental setup.

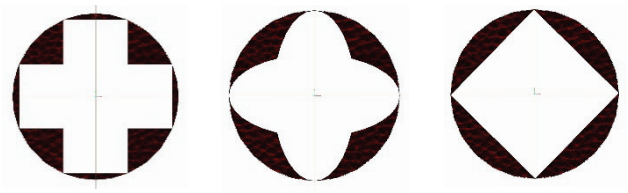

Figure 3. The slot configurations (a) cross (b) oval (c) square.

defines the TLC's bandwidth. The TLC sheet's operating temperature, however, is between the red start (30°C) and the clearing point (46°C); at lower temperatures, the sheet stays black. It is red

between 30° C and 31°C and turns blue in the range between 35°C and 46°C. The clearing point temperature is referred to as turning black again. Thus the local spatial variation of temperature can be obtained by any digitizer and quantified by pixel-specific information. The pixel response corresponding to the temperature is generally available in the RGB color domain. The pixel response in RGB mode needs to be reduced to a single value to relate the temperature.

Calibration of TLC Sheet

The aluminum plate, thin heater, and TLC that need to be calibrated are supported by an acrylic plate measuring 400 mm by 400 mm by 12 mm, which is known as the calibration test plate. As seen in Figure 4, an aluminum plate (0.3 x 0.3 x 0.03 m) has eight grooves in it where thermocouples can be inserted. Eight calibrated K-type thermocouples with thin leads will measure the temperature along the Aluminium plate. The NI 9213 data card is coupled with thermocouple leads and the input module of NI 9213 is connected to the computer system.

The plate is heated incrementally between 30 C and 46 C, and thermocouples and a data collection system are used to record the average temperature. The power supply system's precision control units make it possible to deliver heat in tiny, gradual increments. Once the temperature achieves a constant state, the thermocouples' temperature and the

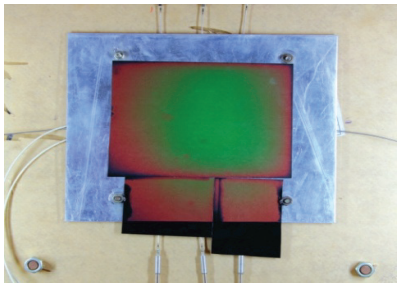

(a) TLC sheet

(b) Aluminium plate with grooves

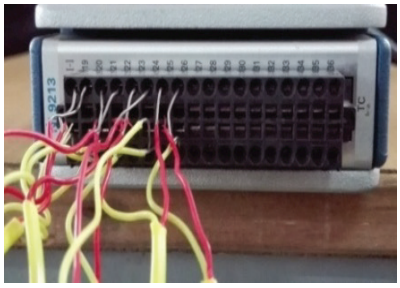

(c) NI 9213 Data acquisition system

(c) Power supply unit

Figure 4. Calibration setup.

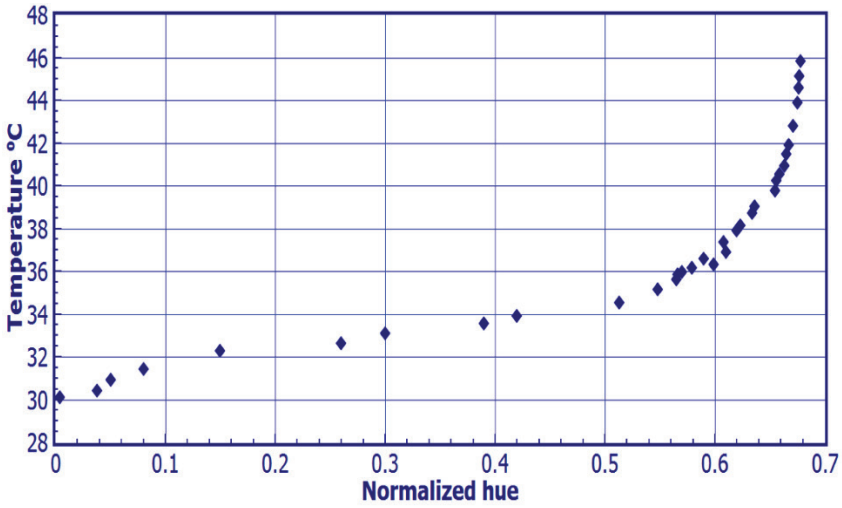

Figure 5. Normalized hue versus temperature for TLC calibration.

TLC's color are simultaneously recorded. The Lab View Vision Assistant module has the TLC picture loaded. Using the Vision Assistant module, the RGB (red, green, and blue) color is converted to the HSI (hue, saturation, and intensity) domain. Gonzalez et al. [18] stated that hue denotes pure color, saturation indicates how much white light has diluted color, and intensity is a measure of brightness. This leads to the plotting and presentation of the color value between TLC with temperature in Figure 5. Temperature is correlated with hue value using a polynomial fit generated from the calibration curve. The temperature is obtained by the values of crystal sheet using the correlation.

Data Reduction

Equations (1) and (2) are used to compute the convective heat transfer coefficient (h) and the Nusselt number (Nu) as given by Nuntadusit et al. [19]

$$h_c = \frac{q_{in}}{(T_w(r) - T_j)} \tag{1}$$

$$Nu = \frac{h_c d_i}{k_a} \tag{2}$$

The heat input is calculated using the equation given by Nanan et al. [20]

$$q_{in} = \frac{V I}{A} \tag{3}$$

The Reynolds number (*Re*) is computed with the equation given by Nanan et al. [20]

$$Re = \frac{U_0 D}{\gamma_a} \tag{4}$$

Where U_0 is the velocity of air in the smooth pipe and γ_a is the kinematic viscosity of air.

Uncertainty Analysis

The Kline-Mc Clintock approach [21] is employed to perform an uncertainty analysis using the equation (5)

$$\Delta R = \left[\left(\frac{\partial R}{\partial m_1}\right)^2 (\Delta\epsilon_1)^2 + \left(\frac{\partial R}{\partial m_2}\right)^2 (\Delta\epsilon_2)^2 + \ldots\ldots \left(\frac{\partial R}{\partial m_n}\right)^2 (\Delta\epsilon_n)^2\right]^{1/2} \tag{5}$$

Convective heat transfer coefficient (h) and other directly measured values are included in the derived quantity (R), which denotes the quantity of interest that must be calculated using a suitable relation. $\Delta\epsilon$ is the measurement error level. Table 1 provides the measured experimental value together with its error levels.

Table 1. Uncertainty in experimental measurements

Parameter	Measured Value	Error level
Voltage, *V*	12.1 V	0.01 V
Current, *I*	1.16 A	0.005 A
Impinging Surface Temperature, T_w	36.26°C	0.2°C
Exit pipe inner diameter, *D*	0.031 m	0.001 m

$$\Delta Nu = \left[\left(\frac{\partial Nu}{\partial q_{in}}\right)^2 (\Delta\epsilon_q)^2 + \left(\frac{\partial Nu}{\partial D}\right)^2 (\Delta\epsilon_D)^2 + \left(\frac{\partial Nu}{\partial T_w(r)}\right)^2 (\Delta\epsilon_{T_w})^2 + \left(\frac{\partial Nu}{\partial T_j}\right)^2 (\Delta\epsilon_{T_j})^2\right]^{\frac{1}{2}} \tag{6}$$

Where, $Nu = \frac{q\, d_i}{k_a (T_w(r) - T_j)}$

$$\Delta Nu = \left[\left(\frac{\partial\left(\frac{q\,d_i}{k(T_w(r)-T_j)}\right)}{\partial q}\right)^2(\Delta\epsilon_q)^2+\left(\frac{\partial\left(\frac{q\,d_i}{k(T_w(r)-T_j)}\right)}{\partial D}\right)^2(\Delta\epsilon_D)^2 + \left(\frac{\partial\left(\frac{q\,d_i}{k(T_w(r)-T_j)}\right)}{\partial T_w(r)}\right)^2(\Delta\epsilon_{T_w})^2+\left(\frac{\partial\left(\frac{q\,d_i}{k(T_w(r)-T_j)}\right)}{\partial T_j}\right)^2(\Delta\epsilon_{T_j})^2\right]^{\frac{1}{2}} \quad (7)$$

The uncertainty in the Nusselt number for circular jet for X/D = 3.5 at L/D = 4 and for Re = 12700 is 3.85%.

NUMERICAL METHODOLOGY

Computational Domain

By solving the equations of fluid and energy with turbulence model as a closure, the numerical results are arrived with the CFX tool. Figure 6a displays the analysis domain employed in this investigation. To carry out flow analysis with varying separation distance, L/D up to 4 is considered. The air is delivered to the impinging surface at a temperature of 30°C. As illustrated in Figure 6a, the boundary conditions are given with Re = 23000. The surfaces where the jet leaves the domain are represented by an unconfined wall with pressure, P = 1 atm.

condition of uniform heat flux. Tetrahedral combined with prism are employed for meshing as shown in Figure 4b. The Table 2 shows the various turbulence models used in the previous literatures.

The second-order high-resolution discretization scheme is used. However, this discretization scheme gives relatively

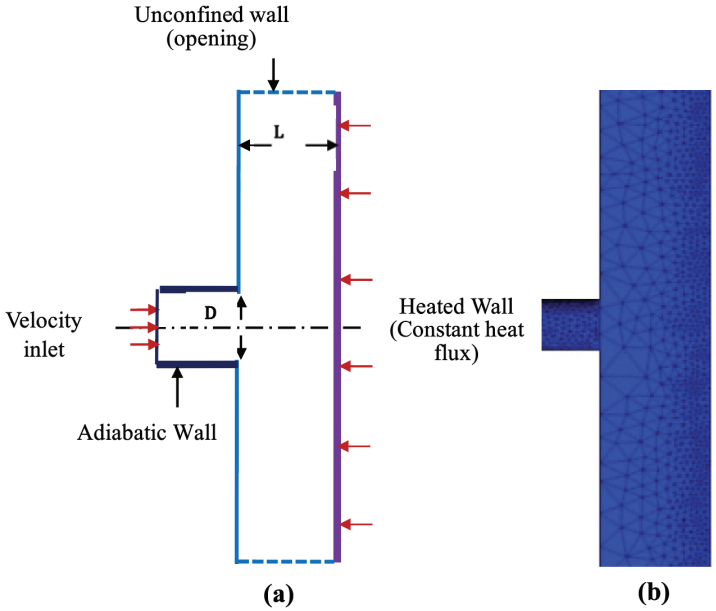

Figure 6. (a) Domain of impingement section (b) Mesh distribution with refined elements at the striking section.

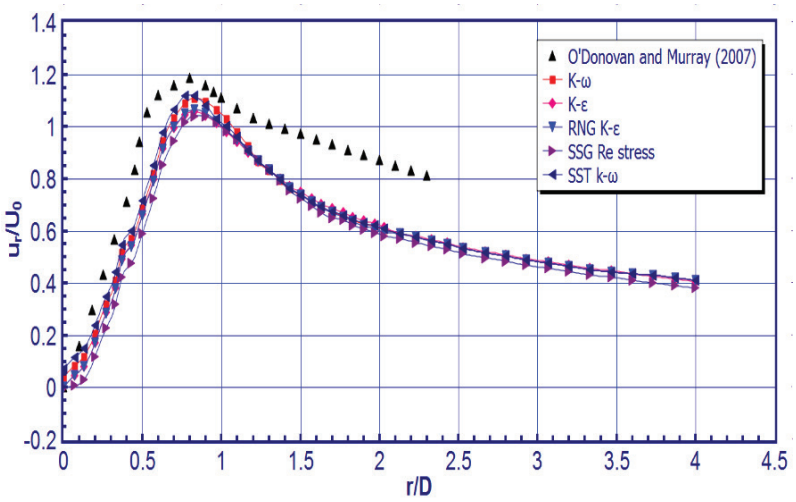

Figure 7. Radial velocity component of circular jet for L/D = 2 at Re = 23000 for different turbulence models.

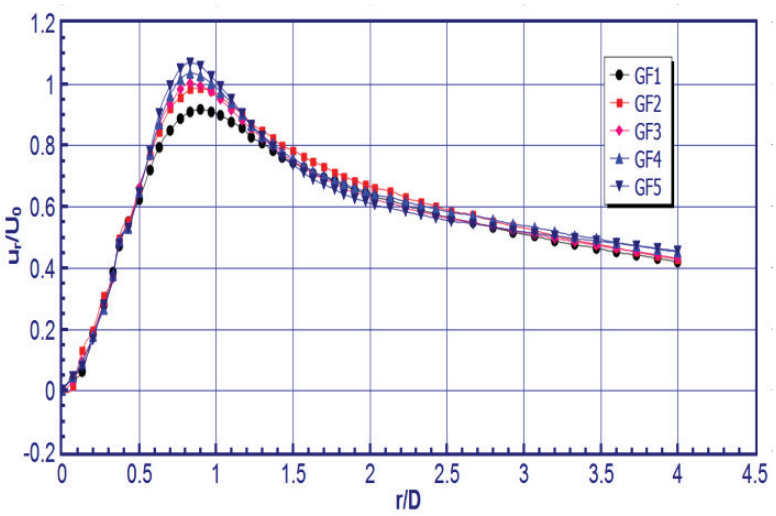

Figure 8. Radial velocity component of circular jet for L/D = 2 at Re = 23000 for varying grid intensity.

precise results than the first-order scheme, it is relatively less stable regarding convergence. To improve the convergence, the solution is primarily attained with first-order upwind discretization with a blend factor of 0 and residual of 10^{-6}. The equations for incompressible flow are given by.

The continuity equation is given by

$$\nabla . \overline{U} = 0 \tag{8}$$

The momentum equation is written as

$$\rho \frac{D\bar{U}}{Dt} = \rho f - \nabla p + \mu \nabla^2 \overline{U} \tag{9}$$

The energy equation can be written as

$$\rho \frac{DE}{Dt} = \frac{\partial Q}{\partial t} + k\nabla^2 \mathrm{T} + \varphi \tag{10}$$

Selection of Turbulence Model

Figure 7 gives the turbulence model obtained in the current analysis comparing the deviation of the radial component of velocity with those experimentally obtained by O'Donovan and Murray [30]. SSG Reynolds stress and

Table 2. Turbulence models and other parameters in numerical analysis on impinging jet

Previous studies	Reynolds number	*L/D*	Turbulence model
Angioletti and Ruocco [23]	1000 - 4000	4.5	RNG *k*-ε, SST *k*-ω, Reynolds stress model
Yang and Tsai [24]	16100 - 29600	4 - 10	*k*-ω model
Sagot et al. [25]	23000	2	SST *k*-ω
Yang et al. [26]	5920 - 23700	0.5 - 12	*k*-ε model
Draksler and Koncar [27]	23000	2	SST *k*-ω
Sharif and Banerjee [28]	5000 - 20000	6 - 8	*k*-ε model
Yang et al. [29]	11000 - 17000	3 - 12	SST *k*-ω

Table 3. Radial component of velocity for varying grid components

Grid factor	No. of Nodes Million	Average ur/Uo	Relative error %
GF1	1.08	0.604	2.58
GF2	2.13	0.608	1.94
GF3	3.49	0.613	1.13
GF4	4.83	0.617	0.48
GF5	6.51	0.620	--

RNG k-ε models however lag in predicting the values in the area of stagnation, the SST k-ω and standard k-ω models managed to calculate the values with an error of 16.43% and 18.76% respectively radially at $0 < r/D < 0.8$. A comprehensive calculation of various turbulence values for slotted air jet study was carried out by Dutta et al. [31] for L/D distances of 4 and 9.2 at Re = 20000. They concluded that the k-ω models (Standard and SST) showed in similarity with physical values in predicting flow and heat parameter at L/D = 4 whereas the standard k-ε model with provided good results with experimental data L/D = 9.2. While the k-ω model (SST) gives fairly good predictions on the separation of flow with intense pressure gradients [32] for flow phenomenon relating to circulation [33]. This model is selected for the current analysis.

Grid Independence

The grid independence of the solution is validated by carrying out a study on grid density. This is done by successive mesh refinement by the meshing element value of 1.08 million to a refined element of 6.51 million air jet. Figure 8 gives the radial velocity parameters for the selected grid elements. The variation is observed radially with r/D values between 0.6 and 0.9. Table 3 shows that the radial velocity variation between the chosen grid elements and a relatively marginal variation is observed between the grid factors GF4 and GF5. Therefore, the grid factor GF4 is used in the present study to keep a balance between computational time and accuracy provided that the size of the domain is not varied.

EXPERIMENTAL RESULTS

Local Heat Transfer Visualization

The TLC images showing the variation of Nusselt values for uniform cross section and slotted air jets are given in Figures 9 and 10. The Nusselt value variation at the mid surface for circular jet means that the existence

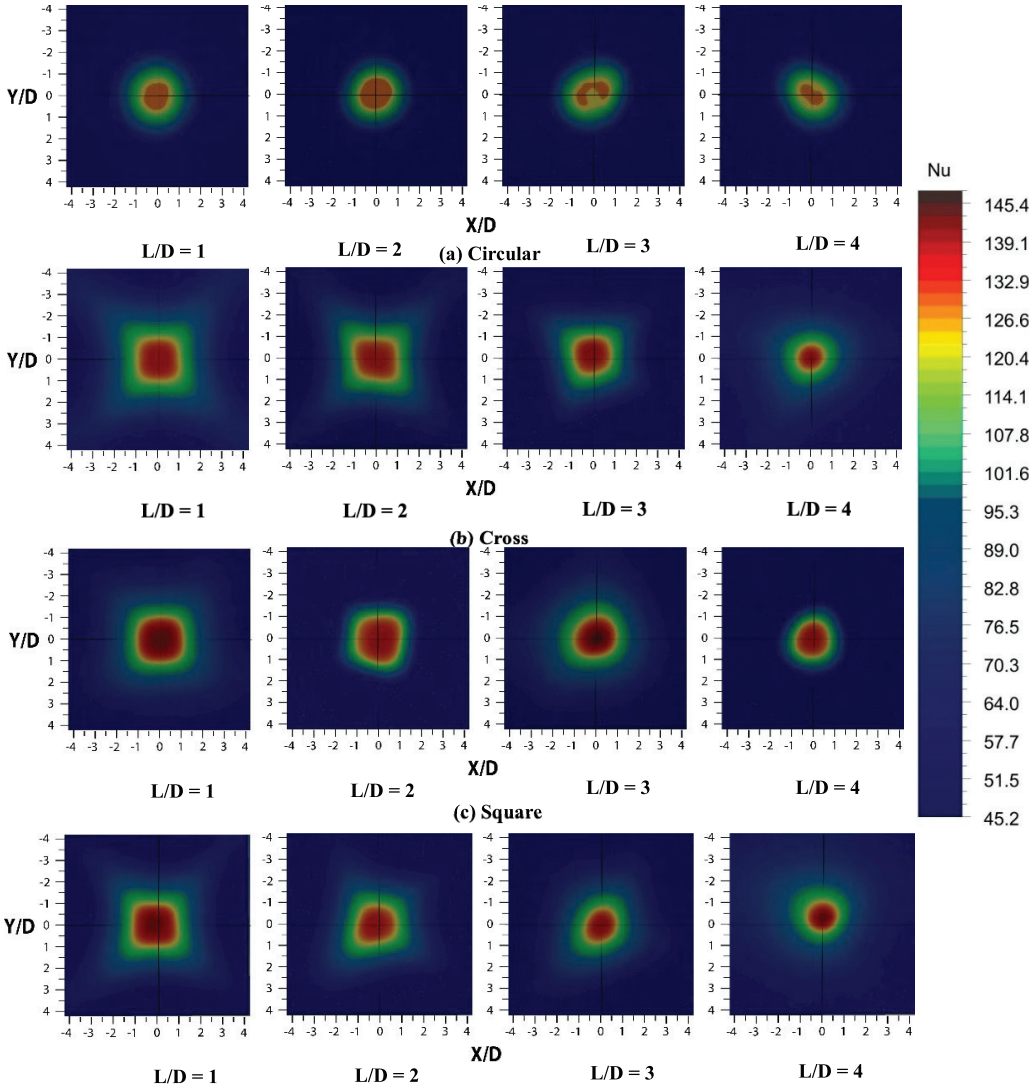

Figure 9. Nusselt number parameter for circular and slotted air jets for L/D = 1- 4 at Re = 12700.

of a core maintains its values of velocity uniform at the outlet and indicates lower jet spread before impingement as shown in

Figure 9 at L/D = 1, conversely the Nusselt value distribution shows that slotted jet transits to turbulent jet with greater jet spread before impingement. However, the variation is marginal among the slotted je at L/D =1 at Re = 12700, the jet spread is notably higher for a square section at Re = 23000 as shown in Figure 10 (c) at L/D =1. In the case of slotted jet distinct zones appear at L/D = 1, indicating that the flow jet leaving the pipe takes the profile of the slot as shown in Figure 9 which is symmetry about both x and y axes. This fact is also reported by Ianiro and Cardone [34] in their study by multi-channel jet at Re = 28000. At L/D = 2 the change in flow pattern coupled with a decrease in Nusselt value is seen for the slotted jet (Figure 9). The results of the circular jet show that the Nusselt number distribution has little dependence on the separation distance as the variation is marginal at L/D = 4 when compared with L/D = 1 and 2, the slotted jet however shows the marked variation of Nusselt value beyond the region X/D = 1.5 on either side. This is attributed to the merging of slotted jets downstream of flow exit with increased separation distance.

The impingement area appears to be broadened with the air jet leaving the square section at all the L/D distances (Figure 10c) however the Nusselt value is not uniform. The Nusselt value further decreases beyond the region X/D = 2 for all the considered cases at L/D = 4, substantiating the weak flux in axial direction of the air jet in the impinged area. Conversely, the Nusselt value at the vicinity of the stagnation area is significantly high for the slotted air jet

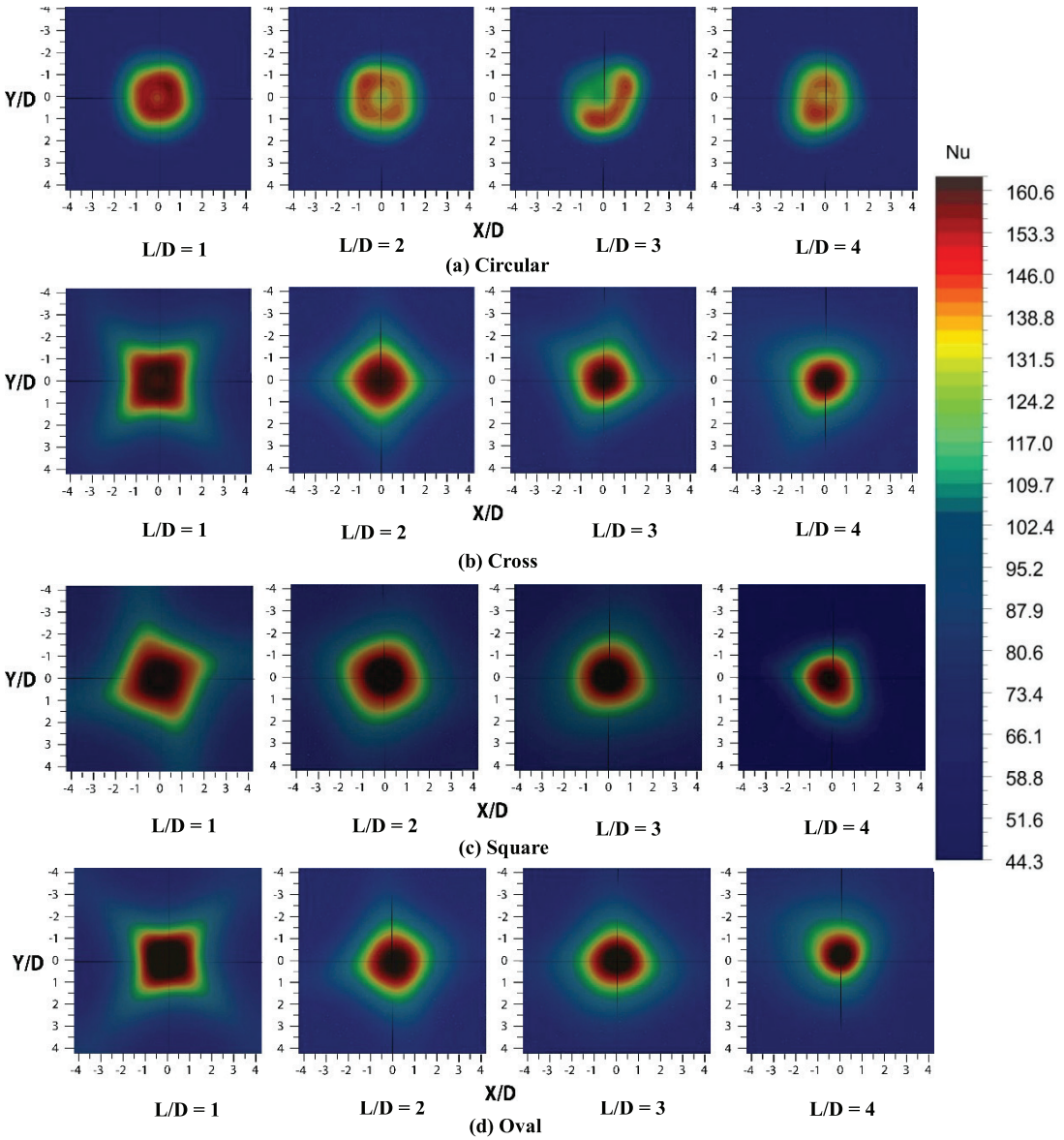

Figure 10. Nusselt number distribution for circular and slotted jets for L/D = 1- 4 at Re = 23000.

even at increased separation distances, this is more intense for the square jet at Re = 23000 as shown in Figure 10c. This fact is reported by Gardon and Akfirat [36] in their study at Re = 22000 stating that increasing the turbulence enables the heat parameter to increase at the stagnation area though jet arrival velocity is falling.

NUMERICAL RESULTS

Axial Velocity Variation

The axial velocity parameter for circular and slotted jets is shown in Figure 11. The axial velocity peak is observed for slotted jets and noticeably higher for square section corresponding to $r/D \approx 0.4$ at L/D = 1 (Figure 11a) and the peak decreases with increased L/D distances. The velocity parameter of the circular jet reduces reaching its maxima with increasing r/D distances but not as rapidly as the slotted jet at all L/D distances. While the velocity peak in the slotted jet is due to the sharp edges creating intensive turbulence as observed by Parham et al. [37] for Re = 23460 at flow exit thereby increasing the velocity at a shorter L/D distance, whereas the lower turbulence circular impinging jet causing the existence of potential core results in a marginal change in velocity at the exit as shown by Viskanta [38] and Alimohammadi et al. [39]. The velocity peak decreases for the slotted jets at L/D = 2 (Figure 11b) nearby stagnation area and the decrease is because of low axial force with increase in separation distance as reported by Ianiro and Cardone [34]. The jet leaving the square section however produces higher axial velocity radially at $0 < r/D < 0.3$ compared with cross and oval sections as well as a circular section at L/D = 2 as presented in Figure 11b. The reduction in velocity parameter at L/D = 3 is marginal comparing with L/D = 2 for the slotted jets and the decrease is significant at L/D = 4 (Figure 11d). On the contrary, while increasing the L/D distances the velocity parameter of the circular jet is not affected in impinging region. This is due to the velocity of the jet coming out of the circular section is uniform with an increase in L/D distance whereas higher turbulence and mixing slotted jet causes low arrival velocity of air jet at the impinging surface.

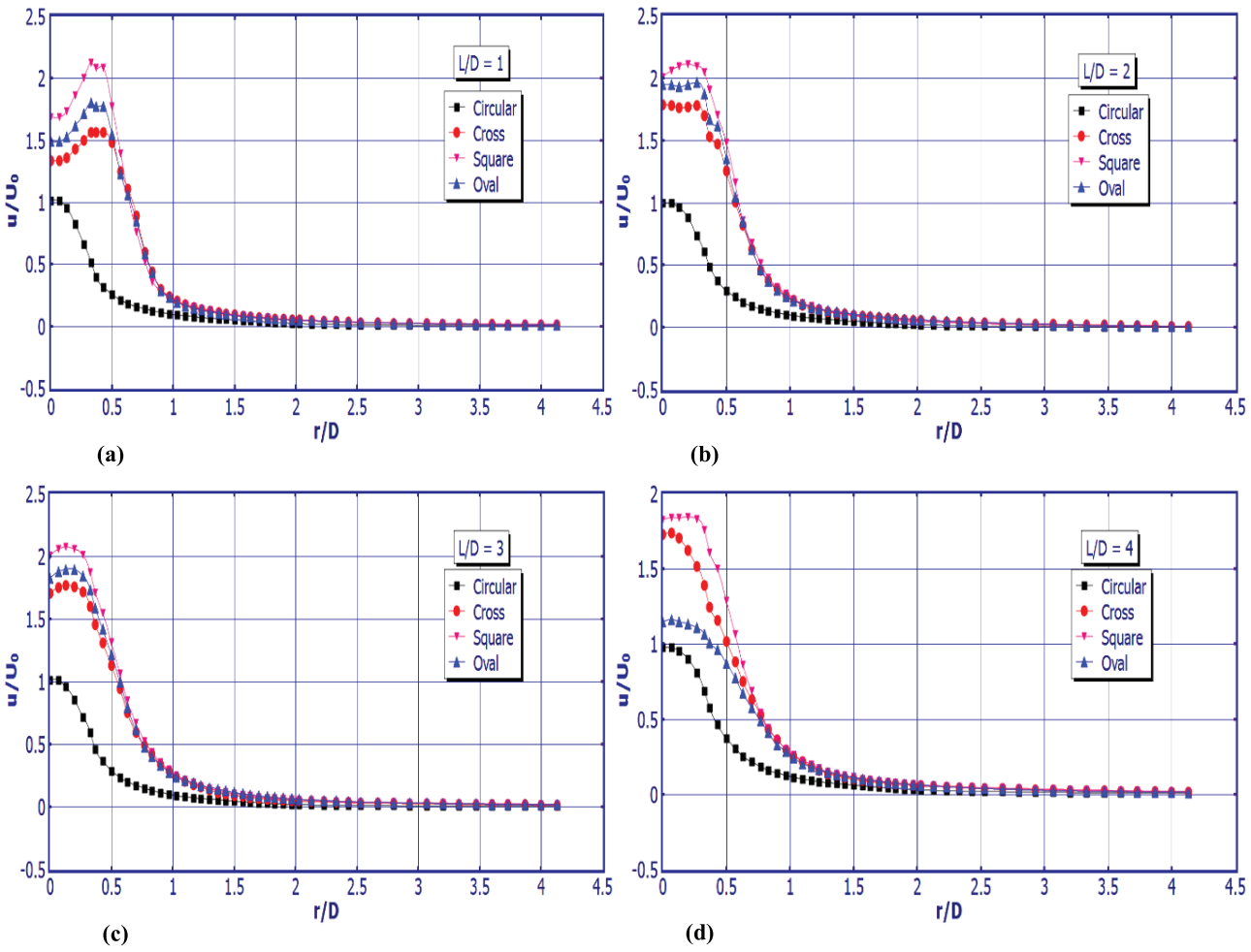

Figure 11. Axial velocity parameter for air jet for L/D = 1- 4 at Re = 23000.

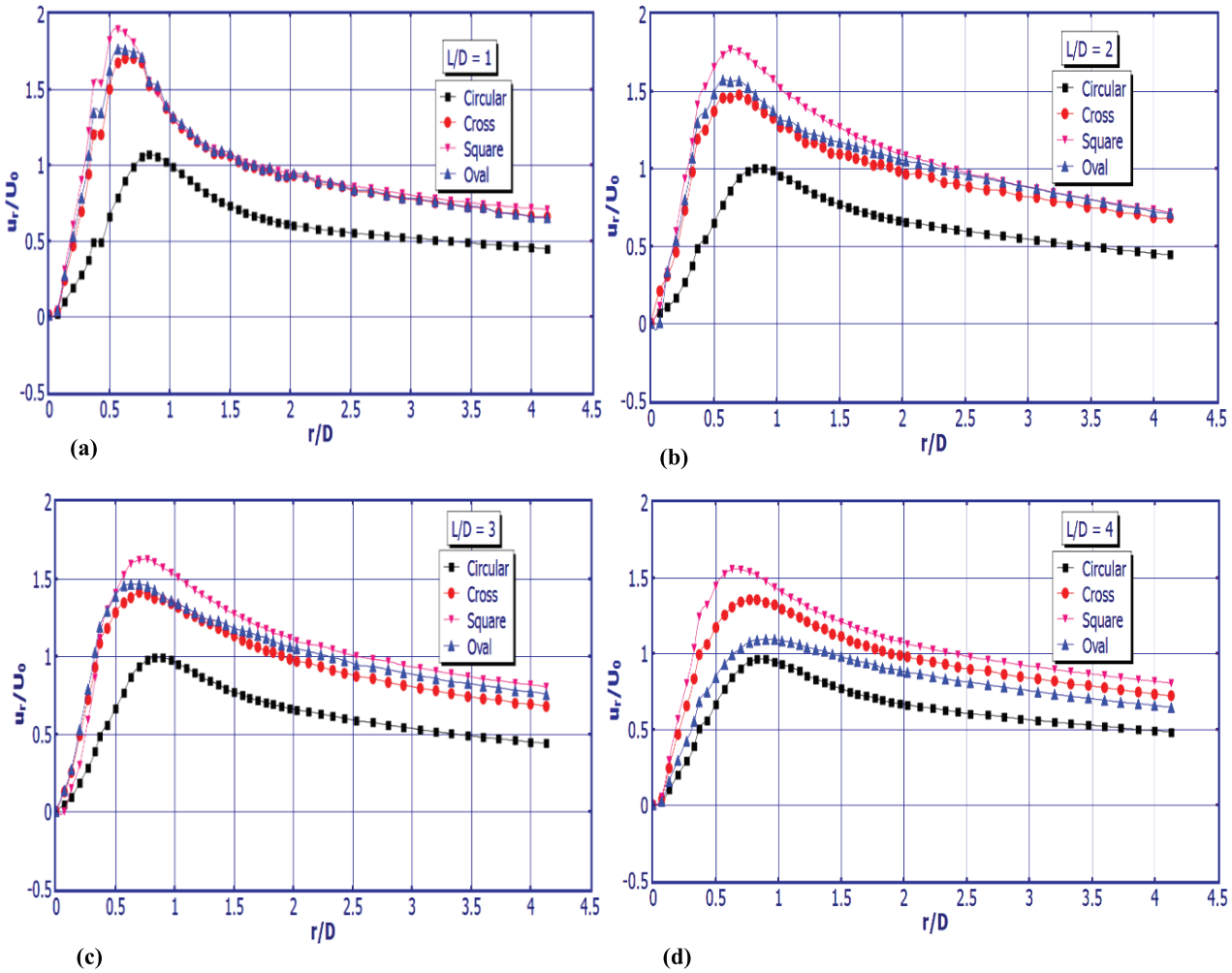

Figure 12. Radial velocity parameter for air jet for L/D = 1- 4 at Re = 23000

Radial Velocity Variation

The radial velocity distribution of slotted and circular jets is shown in Figure 12. The radial velocity near the impinging surface increases at $0 < r/D < 0.81$ and $0 < r/D < 0.6$ for the jets respectively reaching its maximum at L/D = 1 (Figure 12a). The velocity parameter of the air jet coming out of the square section is relatively high at $0.2 < r/D < 0.6$ on comparing with other slotted sections as well as the circular section at L/D = 1 as shown in Figure 12a. However the velocity parameter of the uniform section jet is lower which spreads radially outward at r/D = 0.8 indicating jet spread in impingement area. While the high radial momentum of the slotted jet causes a steep rise in radial velocity whereas the rise is less prominent for the circular jet at L/D = 1 (Figure 12a). The slotted jet radially extends outward at L/D = 2 reaching its maximum with $r/D \approx 0.7$ for square air jets and at $r/D \approx 0.6$ for cross and oval jets. Besides the velocity peak for the slotted jet at L/D = 2 is about 0.2 times lower than which obtained with L/D = 1. The slotted jet radially extends outward at L/D = 2 reaching its maximum with $r/D \approx 0.7$ for square jets and at $r/D \approx 0.6$ with cross and oval air jets. Besides the velocity peak for the slotted jet at L/D = 2 is about 0.2 times lower than which obtained with L/D = 1. The extending of air jet at L/D = 2 (Figure 12b) is attributed to the sufficient room to spread at increased separation distance.

While the location of maxima shifts away radially at L/D = 3 for the slotted jet with further reduction in velocity peak as shown in Figure 12c, whereas it is marginal for the circular jet. The slotted jet further moves away at L/D = 4 broadening the impingement region with a lower value in magnitude (Figure 12d). The air jet leaving the square section maintains its original momentum resulting in higher average velocity distribution at L/D = 4 compared with cross and oval sections.

Velocity Vectors

The velocity vectors for the circular and slotted jet are shown in Figure 13. The potential core is evident for the circular and slotted air jet is evident at L/D = 1 (Figure 13a, e, i, m) as the fluid stream moves without any disturbance in

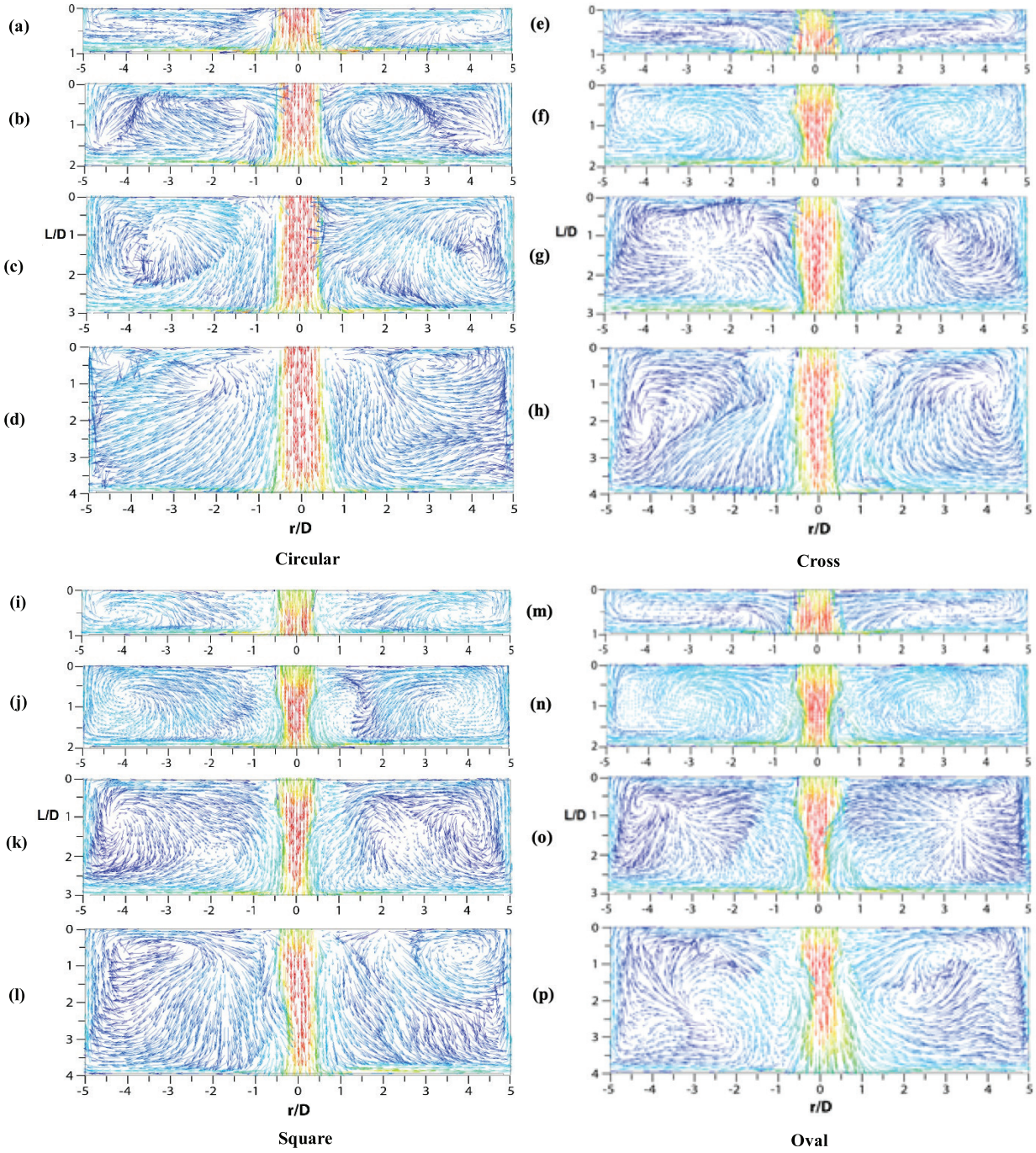

Figure 13. Velocity vector distribution for air jets for L/D = 1- 4 at Re = 23000.

the free air flow area. The jet flow interaction of atmosphere creates the cross-flow. The cross-flow effect decreases at L/D = 2 with recirculation zones affecting the potential core area for the slotted jet at flow downstream as shown in Figure 13f, j, and n.

However, the potential core for circular jet remains unaffected as shown in Figure 13b (L/D = 2). The reverse flow develops and interacts near the outer layer of the jet at upstream of the pipe exit thereby increasing the turbulence for the slotted jet as shown in Figure 13f, j, and n whereas the jet leaving the circular section directly impinges on the target plate at L/D = 2. While the main jet of square and oval section (Figure 13l, p) is slightly moving outward with the presence of larger vortices at L/D = 4, whereas the flow leaving circular and cross sections (Figure 13d, h) remains unaffected by the vortices.

Intensity of Turbulence

The mean turbulence intensity for the circular and slotted jet is shown in Figure 14. While the magnitude of

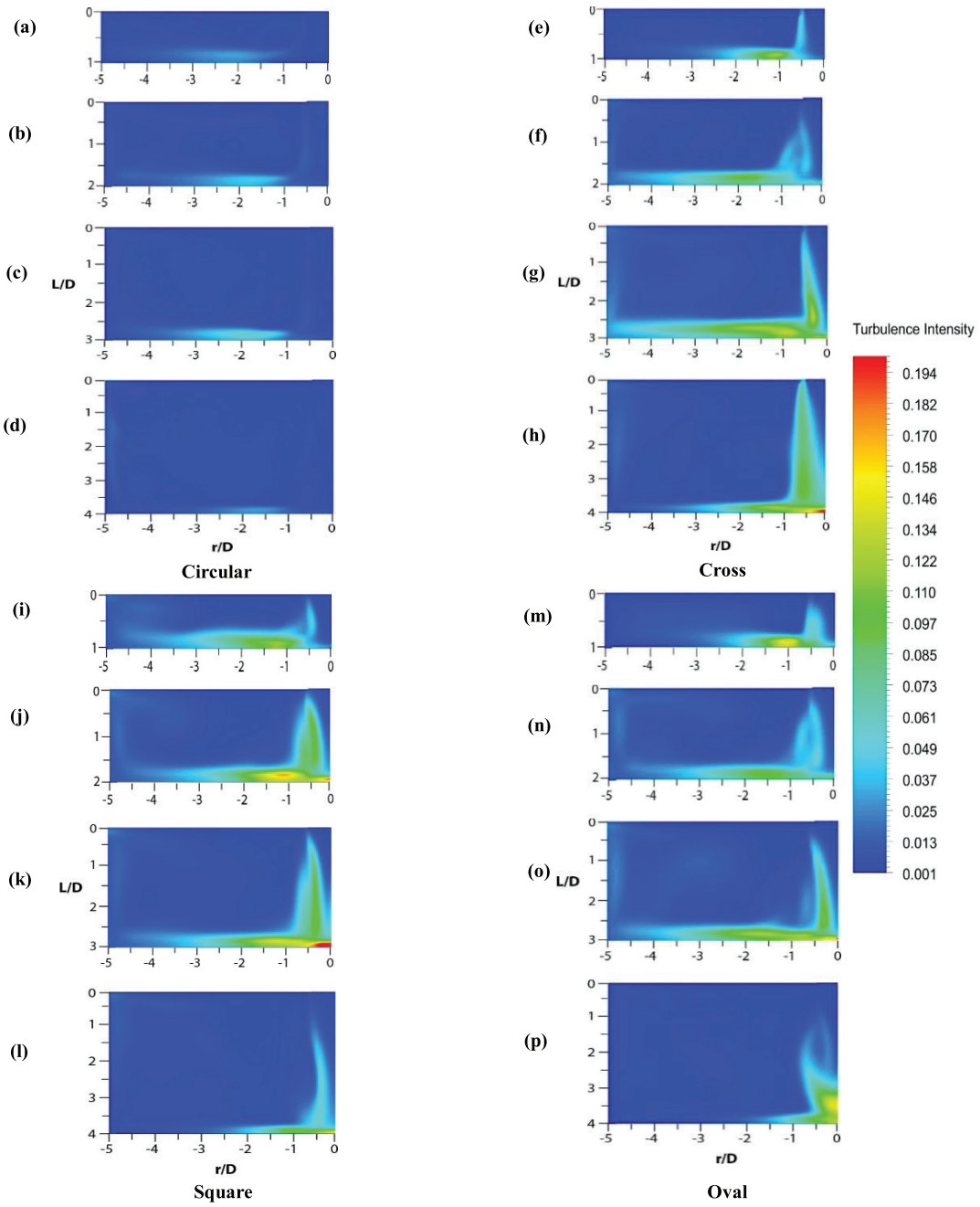

Figure 14. Intensity of turbulence for slotted and circular jets for L/D = 1- 4 at Re = 23000.

turbulence is marginal for the circular air jet, the higher spreading of jet for the slotted jet provides larger turbulence in vicinity of wall jet. The air jet deflected upon leaving the pipe forming an intense turbulence that extends in wall jet area at L/D = 1 as presented in Figure 14e, i, and m. The deflection is maximum as it can be seen moving towards higher r/D values on comparing with uniform section air jet. On comparison, turbulence level in jet area extends in the area at $0 < r/D < 2$ for cross and oval jets (Figure 14e, m) and it is $0 < r/D < 3$ (Figure 14i) for the square jet at L/D =1. The intensity of turbulence is maximum in the area at $1.5 < r/D < 3$ for the circular air jet at L/D = 1 (Figure 14a) and its intensity decreases rapidly beyond that region. This fact is due to higher axial momentum with relatively lower velocity fluctuations of circular air jet. The turbulence level is higher for slotted air jet possibly with existence of shear at L/D = 2 and 3. This fact may enhance the possibility of recirculating flows associated with turbulent intensities. The turbulence distribution pattern is similar however with an increase in magnitude at L/D = 3 for circular as well as slotted jets. This fact is due to the sufficient room for the jet to spread near the target surface probably less at L/D =

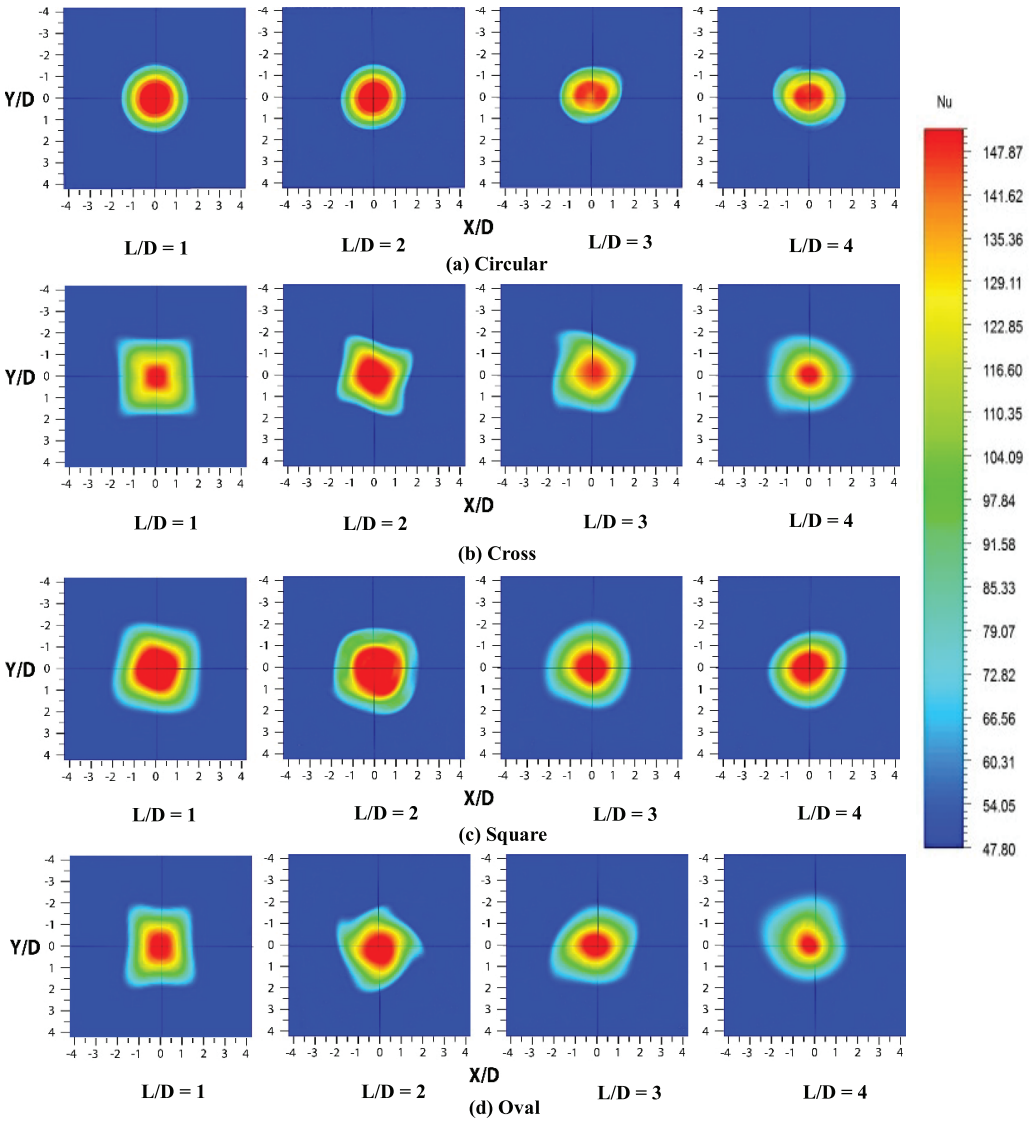

Figure 15. Nusselt number parameter for air jet for L/D = 1- 4 at Re = 12700.

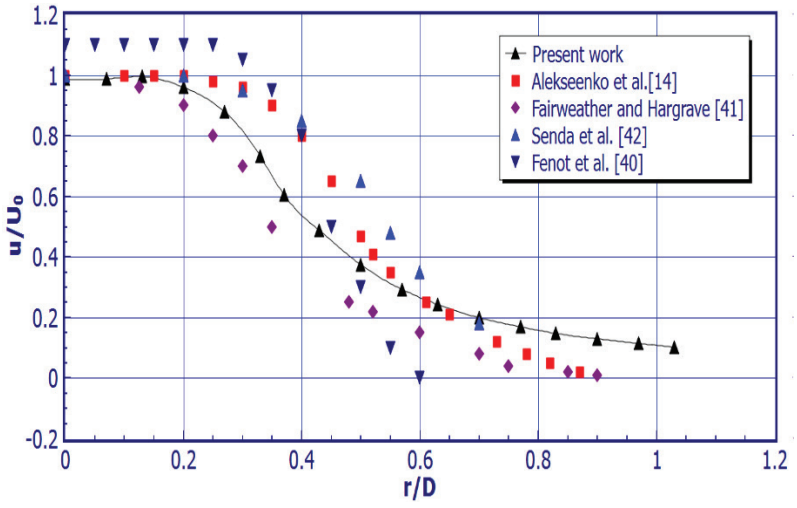

Figure 16. Axial velocity parameter of circular air jet for L/D = 2 at Re = 23000.

1 and 2. The result (Figure 14g, k, o at L/D = 3) indicates that a greater rate of turbulence kinetic energy formed at jet exit transformed into a significant increase in turbulence intensity. However, it does not go beyond the wall jet area for square and oval jets (Figure 14k, o) at L/D = 3, whereas the intensity extends to the wall jet region for the cross jet (Figure 14g). The main jet approaching the surface for the square and oval sections (Figure 14l, p) does not move to the area of jet possibly with their reduced momentum at L/D = 4. However, the mean turbulence value remains high for the cross jet (Figure 14h) and consequently marked effect on vicinity of the target plate compared to square and oval sections.

Nusselt Number Variation

The Nusselt value variation computed by numerical analysis is shown in Figure 15. The Nusselt value distribution at the mid of the uniform section air jet (Figure 15a) reveals minimum jet spread with the existence of potential core which is in agreement the experimental results obtained in Figure 9a. While the Nusselt number distribution has marginal dependence on separation distance for the circular jet as the variation is marginal at L/D = 4, the slotted jet shows significant variation on the impinging region. The Nusselt value close to the zero velocity area is relatively greater for the slotted air jet at L/D = 3 and 4 which are comparable with experimental results shown in Figure 9b-d.

COMPARISON OF RESULTS

Since the selection of a particular slot configuration considerably influencing the flow and heat parameter, the obtained values of axial velocity (u/U_0) for the circular air jet at L/D = 2 is compared with previous studies as shown in Figure 16. The values of (u/U_0) are varying between 0.1 and 0.98 in the area with r/D values between 0 and 1.03. The higher values of axial velocity are observed with r/D values between 0 and 0.37 for Fenot et al. [40]. The current values and the findings of Fairweather and Hargrave [41] and Sendaet al. [42] are fairly comparable in the stagnation as well in impinging regions. The relative error is 13.51% when compared to the mean values found in the literature, and it corresponds to the region where 0 < r/D < 0.9.

CONCLUSION

Experimental and numerical analysis were done on the slotted impinging jet heat transfer and flow properties. The analysis leads to the following conclusions,

- The existence of potential core for circular air jet causing marginal variation of Nusselt value distribution at L/D = 4 compared to L/D = 1 and 2 whereas the slotted jet shows marked variation of Nusselt (136.8 at L/D = 1, 135.2 at L/D = 2 and 113.5 at L/D = 4) at X/D = 1.5.
- The Nusselt value at 0 < X/D < 0.5 is higher in the range varying between 127.8 and 167.9 for the slotted jet even at increased separation distances compared with the circular jet.
- The impingement section is more extended for square jet corresponding to X/D = 3, 2.5, and 1.75 at L/D = 1, 2, and 3 respectively with relatively higher Nusselt number in the range of (Nu = 117 – 167.9 compared with circular, cross and oval jets
- The key finding on flow structure reveal that the square jet exhibits higher axial velocity peak (u/U_0 = 2.124) in the area at r/D varies between 0 and 0.5 for Nozzle to plate distance = 1 and the peak decreases progressively with increasing separation distance and reaching its minimum at u/U_0 = 1.729 for L/D = 4.
- The axial velocity parameter of the circular air jet is not affected by increased separation distances. The square jet exhibits relatively higher average radial velocity (u_r/U_0 = 1.31) substantiating its higher momentum in the at r/D values between 0.5 and 1.5.
- The highest values of turbulence intensity (TI = 0.206) is observed at r/D = 0.5 for the square air jet at L/D = 3
- The presence of reverse flow at the outer layer of the jet exit is observed for the square and cross jets at r/D = 0.4 and even at increased separation distances (L/D = 3 and 4) which enhances the entrainment of ambient air.

NOMENCLATURE

A	Impingement surface area m^2
D	Outlet diameter of pipe, m
L/D	Dimensionless distance between outlet of air jet and target surface
h	Air side heat transfer coefficient, W/m^2 K
Ka	Thermal conductivity, W/m K
Nu	Nusselt number
Re	Reynolds number
r/D	Dimensionless radius measured on the target plate
q_{in}	Heat flux, W/m^2
$T_{w(r)}$	Temperature on target plate at r distance from the mid surface of the target plate, K
T_j	Temperature of outlet air at smooth pipe, K
T_a	Ambient temperature, K

AUTHORSHIP CONTRIBUTIONS

Conceptualization, Methodology, Resources, Formal analysis and investigation – S. Mohamed Illyas, B.R.Ramesh Bapu and A. Muthu Manokar. Writing, review and editing – S. Mohamed Illyas, B.R.Ramesh Bapu and A. Muthu Manokar.

DATA AVAILABILITY STATEMENT

The data supporting the findings of study is provided in the article, according to the authors. The corresponding

author can provide the raw data supporting the findings of the study upon reasonable request.

CONFLICT OF INTEREST

No possible conflicts of interest exist that the author disclosed about writing or publication of this paper.

ETHICS

Regarding the writing and publication of this manuscript, the author has not declared any potential conflicts of interest.

REFERENCES

[1] Wang L, Feng LH, Xu YI, Xu YA, Wang JJ. Experimental investigation on flow characteristics and unsteady heat transfer of noncircular impinging synthetic jets. Int J Heat Mass Transf 2022;190:122760. [CrossRef]

[2] Zhu J, Dou R, Hu Y, Zhang S, Wang X. Heat transfer of multi-slot nozzles air jet impingement with different Reynolds number. Appl Therm Engineer 2021;186:116470. [CrossRef]

[3] Afroz F, Sharif MAR. Numerical investigation of heat transfer from a plane surface due to turbulent annular swirling jet impingement. Int J Therm Sci 2020;151:106257. [CrossRef]

[4] Fenot M, Dorignac E, Lantier R. Heat transfer and flow structure of a hot annular impinging jet. Int J Therm Sci 2021;170:107091. [CrossRef]

[5] Yadav S, Saini RP. Numerical investigation on the performance of a solar air heater using jet impingement with absorber plate. Sol Energy 2020;208:236−248. [CrossRef]

[6] Mohammed AA, Razuqi SA. Effect of air fan position on heat transfer performance of elliptical pin fin heat sink subjected to impinging air flow. J Therm Engineer 2021;7:1406−1416. [CrossRef]

[7] Badiger B, Katti VV, Anil TR. Experimental investigation of heat transfer characteristics of an inverse diffusion flame in a coaxial tube burner for with and without swirl. J Therm Engineer 2022;8:67−77. [CrossRef]

[8] Mohammed AA, Razuqi SA. Performance of rectangular pin-fin heat sink subject to an impinging air flow. J Therm Engineer 2021;7:666−676. [CrossRef]

[9] Lee D H, Song J, Jo MC. The effects of nozzle diameter on impinging jet heat transfer and fluid flow. J Heat Transf 2004;126:554−557. [CrossRef]

[10] Katti V, Prabhu SV. Experimental study and theoretical analysis of local heat transfer distribution between smooth flat surface and impinging air jet from a circular straight pipe nozzle. Int J Heat Mass Transf 2008;51:4480-4495. [CrossRef]

[11] Yan WM, Mei SC, Liu HC, Soong CY, Yan WJ. Measurement of detailed heat transfer on a surface under arrays of impinging elliptic jets by a transient liquid crystal technique. Int J Heat Mass Transf 2004;47:5235−5245. [CrossRef]

[12] Lytle D,Webb BW. Air jet impingement heat transfer at low nozzle-plate Spacings. Int J Heat Mass Transf 1994;37:1687−1697. [CrossRef]

[13] Sezai I, Mohamad AA. Three-dimensional simulation of laminar rectangular impinging jets, Flow structure and heat transfer. J Heat Transf 1999;121:50−56. [CrossRef]

[14] Alekseenko SV, Bilsky AV, Dulin VM, Markovich DM. Experimental study of an impinging jet with different swirl rates. Int J Heat Fluid Flow 2007;28:1340-1359. [CrossRef]

[15] Ianiro A, Cardone G. Heat transfer rate and uniformity in multichannel swirling impinging jets. Appl Therm Engineer 2012;49:89-98. [CrossRef]

[16] Zuckerman N, Lior N. Jet impingement heat transfer: Physics, correlations, and numerical modeling. Adv Heat Transf 2006;39:565−631. [CrossRef]

[17] Mehta RD. The aerodynamic design of blower tunnels with wide - Angle diffusers. Progress Aerospace Sci 1979;18:59−120. [CrossRef]

[18] Gonzalez RC, Woods RE, Eddins SL. Digital Image Processing Using MATLAB. New York: McGraw Hill; 2013.

[19] Nuntadusit C, Waehayee M, Bunyajitradulya A, Eiamsa-ard S. Visualization of flow and heat transfer characteristics for swirling impinging jet. Int Commun Heat Mass Transf 2012;39:640−648. [CrossRef]

[20] Nanan K, Wongcharee K, Nuntadusit C, Eiamsa-ard S. Forced convective heat transfer by swirling impinging jets issuing from nozzles equipped with twisted tapes. Int Comm Heat Mass Transf 2012;39:844-852. [CrossRef]

[21] Holman JP. Heat Transfer Eight SI Metric Edition. New York: McGraw- Hill; 2002.

[22] John CT, Anderson D, Pletcher RH. Computational Fluid Mechanics Heat Transfer. Abington, UK: Taylor and Francis; 1997.

[23] Angioletti ME, Ruocco GN. CFD turbulent modeling of jet impingement and its validation by particle image velocimetry and mass transfer measurements. Int J Therm Sci 2005;44:349−356. [CrossRef]

[24] Yang YT, Tsai SY. Numerical study of transient conjugate heat transfer of a turbulent impinging jet. Int J Heat Mass Transf 2007;50:799−807. [CrossRef]

[25] Sagot B, Antonini G, Christgen A, Buron F. Jet impingement heat transfer on a flat plate at a constant wall temperature. Int J Therm Sci 2008;47:610−1619. [CrossRef]

[26] Yang YT, Wang YH, Hsu JC. Numerical thermal analysis and optimization of a water jet impingement cooling with VOF two phase approach. Int Comm Heat Mass Transf 2015;68:162−171. [CrossRef]

[27] Draksler M, Koncar B. Analysis of heat transfer and flow characteristics in turbulent impinging jet. Nucl Engineer Des 2011;241:1248−1254. [CrossRef]
[28] Sharif MAR, Banerjee A. Numerical analysis of heat transfer due to confined slot jet impingement on a moving plate. Appl Therm Engineer 2009;29:532−540. [CrossRef]
[29] Yang YT, Wei TC, Wang YH. Numerical study of turbulent slot jet impingement cooling on a semi-circular concave surface. Int J Heat Mass Transf 2011;54:482−489. [CrossRef]
[30] O'Donovan TS, Murray DB. Jet impingement heat transfer - Part I: Mean and root mean square heat transfer and velocity distributions. Int J Heat Mass Transf 2007;50:3291−3301. [CrossRef]
[31] Dutta R, Dewan A, Srinivasan B. Comparison of various integration to wall (ITW) RANS models for predicting turbulent slot jet impingement heat transfer. Int J Heat Mass Transf 2013;65:750−764. [CrossRef]
[32] ANSYS. Ansys CFX Solver modeling guide. Available at: https://dl.cfdexperts.net/cfd_resources/Ansys_Documentation/CFX/Ansys_CFX-Solver_Modeling_Guide.pdf. Accessed Aug 7, 2024.
[33] Liu Z, Li J, Feng Z. Numerical study of swirl cooling in a turbine blade leading edge model. J Therm Phys Heat Transf 2015;29:66−178. [CrossRef]
[34] Ianiro A, Cardone G. Heat transfer rate and uniformity in multichannel swirling impinging jets. Appl Therm Engineer 2012;49:89−98. [CrossRef]
[35] Yang HQ, Kim T, Lu TJ, Ichimiya K. Flow structure, wall pressure and heat transfer characteristics of impinging annular jet with/without steady swirling. Int J Heat Mass Transf 2010;53:4092−4100. [CrossRef]
[36] Gardon R, Akfirat JC. The role of turbulence in determining the heat-transfer characteristics of impinging jets. Int J Heat Mass Transf 1965;8:1261−1272. [CrossRef]
[37] Parham K, Esmaeilzadeh E, Atikol U, Aldabbagh LBY. A numerical study of turbulent opposed impinging jets issuing from triangular nozzles with different geometries. Heat Mass Transf 2011;47:427−437. [CrossRef]
[38] Viskanta R. Heat transfer to impinging isothermal gas and flame jets. experiment Therm Fluid Sci 1993;6:111−134. [CrossRef]
[39] Alimohammadi S, Murray BD, Persoons T. Experimental validation of a computational fluid dynamics methodology for transitional flow heat transfer characteristics of a steady impinging jet. J Heat Transf 2014;136:091703. [CrossRef]
[40] Fenot M, Dorignac E, Lalizel G. Heat transfer and flow structure of a multichannel impinging jet. Int J Therm Sci 2015;90:323−338. [CrossRef]
[41] Fairweather M, Hargrave GK. Experimental investigation of an axi symmetric, impinging turbulent jet. 1. Velocity field. Experiment Fluids 2002;33:464-471. [CrossRef]
[42] Senda M, Inaoka K, Toyoda D. Sato S, Heat transfer and fluid flow characteristics in a swirling impinging jet. Heat Transf Asian Res 2005;34:324−335. [CrossRef]